Journal of Catalysis 418 (2023) 151–162

Contents lists available at ScienceDirect

Journal of Catalysis

journal homepage: www.elsevier.com/locate/jcat

Regulating CeO_2 morphologies on the catalytic oxidation of toluene at lower temperature: A study of the structure–activity relationship

Youcai Zhu [a], Caiting Li [a,*], Caixia Liang [a], Shanhong Li [a], Xuan Liu [a], Xueyu Du [a], Kuang Yang [a], Jungang Zhao [a], Qi Yu [a], Yunbo Zhai [a], Ying Ma [b]

[a] College of Environmental Science and Engineering, Key Laboratory of Environmental Biology and Pollution Control (Ministry of Education), Hunan University, Changsha 410082, PR China
[b] Yonker Environmental Protection Co., Ltd, Changsha 410330, PR China

ARTICLE INFO

Article history:
Received 27 September 2022
Revised 10 January 2023
Accepted 11 January 2023
Available online 13 January 2023

Keywords:
Toluene oxidation
CeO_2 material
Lattice oxygen
Oxygen vacancy
Mechanism
Cyclic regeneration

ABSTRACT

Developing efficient and stable non-noble metal catalysts for the catalytic oxidation of volatile organic compounds (VOCs) has always been key for controlling air pollution. For this, cerium dioxide (CeO_2) is a potential material and its morphology has a significant impact on the catalyst performance. Herein, three types of CeO_2 with different morphologies were prepared using the hard template method and successfully applied to toluene oxidation. The CeO_2 nanoparticles catalyst (CeO_2-NP) exhibited the highest efficiency, excellent water resistance, long-term stability, and cycle regeneration. Notably, the activation and migration of lattice oxygen can be facilitated by increasing the temperature, and the oxygen vacancies on the surface of the catalyst can further promote the process. In addition, the oxidation behavior of toluene over the CeO_2-NP catalyst was comprehensively understood by in situ diffuse reflectance infrared Fourier transform spectroscopy (In situ DRIFTS) combined with density functional theory (DFT). It was found that the ring-opening reaction is an essential rate-controlling step. Thus, this study provides a new strategy for exploring mono-metal catalysts with high catalytic performances for the oxidation of VOCs and other pollutants.

1. Introduction

Organic solvents are the major components of products such as paints, adhesives, automobile manufacturing, leather tanning, and oil refining, and are widely used in many aspects of life, especially driven by rapid industrialization [1]. However, using large amounts of organic solvents inevitably results in the emission or leakage of volatile organic compounds (VOCs), which causes many environmental issues and threats to human health.

As one of the typical VOCs pollutants, toluene has attracted more and more attention. Among various control technologies for toluene (including physical adsorption, photocatalysis, thermal decomposition, plasma, biodegradation, and catalytic oxidation, etc.), catalytic oxidation is considered one of the most economical and environmentally friendly control technologies because of its lower reaction temperature, high conversion, and low energy consumption [2–5]. High-performance catalysts have always been the research focus in catalytic oxidation technology. Generally, the performance of non-noble metal catalysts used for the catalytic oxidation of toluene is inferior to that of noble metal-based catalysts [6–10]. However, compared to noble metal-based catalysts, non-noble metal-based catalysts have many advantages, such as low cost, promising activity, sintering resistance, good stability, and high resistance to poisons [11–14]. Therefore, there is an urgent need to develop non-noble metal-based catalysts with high performances to substitute noble metal-based catalysts for the oxidation of toluene at low temperatures.

However, it is still challenging to use a mono-metal catalyst for the effective catalytic oxidation of toluene at low temperatures, it has been found that the active components, element valence, crystal structure, oxygen vacancy, and morphology are closely related to the catalytic performance of the catalysts [15–17]. CeO_2 is one of the best choices among non-noble metal components because of its excellent oxygen storage-release ability and preferability for the formation of oxygen vacancies [18–20]. The morphology of CeO_2 has a great effect on the oxidation of toluene and it has been extensively studied by many researchers. For example, Mi et al. [21] studied CeO_2 with different morphologies and believed that CeO_2 nanopolyhedra had the advantage of more surface lattice oxygen, which was more conducive to catalytic oxidation of toluene. However, Ismail et al.[22] pointed out that the CeO_2 with

* Corresponding author.

https://doi.org/10.1016/j.jcat.2023.01.012
0021-9517/

shuttle morphology has a large specific surface area and surface oxygen vacancy may be the main reason for promoting the oxidation of toluene. In fact, rational regulation of oxygen vacancies and active sites in cerium-based materials has been a research hotspot. Earlier, López et al. [23] explored the influence of modification of synthetic route on the physicochemical properties of nanostructured ceria, and found that the concentration of surface defects and the exposed crystal surface planes are the main reason for the improvement of catalytic activity for toluene oxidation. However, the catalytic activity of CeO_2 still needs to be further improved at lower temperatures (<200 ℃) to meet the needs of industrial applications. In addition, Heredia et al. [24] considered that the (1 1 1) crystal plane of CeO_2 is the more active CeO_2 surface in the catalytic oxidation of toluene by FTIR and DFT studies. Therefore, if the active crystal plane (1 1 1) of CeO_2 can be improved and the oxygen vacancy concentration on the catalyst surface can be increased by regulating the catalyst morphology (such as PMMA template method), the low-temperature catalytic performance of the catalyst will be greatly promoted.

In this study, three CeO_2 materials with different morphologies were successfully prepared and used for the oxidation of toluene. The structure–activity relationship of the catalyst was systematically studied using various characterization methods (Raman, EPR, XPS, H_2-TPD, and O_2-TPD). In addition, the effects of water vapor, O_2 content, toluene concentration, and selective catalytic reduction (SCR) atmosphere on the toluene oxidation were investigated. The effect of temperature on the oxygen species on the CeO_2-NP surface during the catalytic reaction was studied by XPS. Furthermore, the reaction mechanism of CeO_2-NP was investigated using in situ DRIFTS and DFT. Finally, the stability of the toluene oxidation and the recycling of the catalysts were systematically investigated.

2. Experimental section

2.1. Reagents and chemicals

Methyl methacrylate, lauryl sodium sulfate, potassium peroxydisulfate, cerium nitrate hexahydrate, toluene, ethanol, and polyethylene glycol (11 000) were all analytical grade (>99%) and purchased from Sinopharm Chemical Reagent Co., Ltd. All gases (O_2, N_2, NO, and NH_3) were of high purity (99.999%) and purchased from Changsha Rizhen Gas Co., Ltd. Deionized water was produced using water purification system.

2.2. Materials

2.2.1. Preparation of PMMA

PMMA with different morphologies was prepared using a previously reported method with some modifications [25]. For detailed preparation methods, please refer to the Supplementary Material.

2.2.2. Preparation of CeO_2-NP

In this study, 20 mmol $Ce(NO_3)_3{\cdot}6H_2O$ and 20 mmol polyethylene glycol (11 000) were mixed in 10 mL ethanol (40 wt%) and magnetically stirred for 2 h to form a transparent homogeneous mixture solution. The PMMA-UO (5.0 g) was impregnated in the above transparent solution for 6 h before the excess solution was removed via vacuum filtration. The obtained powder was collected and dried at 50 °C for 48 h. The sample was then heated from 50 to 300 °C at a rate of 1 °C·min^{-1}, kept for 3 h in pure N_2, and allowed to cool naturally. Finally, to ensure that the PMMA hard template was completely removed, the sample was heated to 500 °C at a rate of 1 °C·min^{-1} and maintained for 3 h in air. The obtained sample with a nanoparticle (NP) structure was denoted as CeO_2-NP.

2.2.3. Preparation of CeO_2-3DOM

$Ce(NO_3)_3{\cdot}6H_2O$ (20 mmol) was dissolved in 10 mL of a mixed solution of methanol and ethylene glycol (ratio 3:1) and magnetically stirred for 2 h to form a transparent homogeneous mixture solution. The PMMA-O (5.0 g) was impregnated in the above transparent solution for 6 h before the excess solution was removed by vacuum filtration. The obtained powder was collected and dried at 50 °C for 48 h. The sample was then heated from 50 to 300 °C at a rate of 1 °C·min^{-1}, kept for 3 h in pure N_2, and allowed to cool naturally. Finally, to ensure that the PMMA hard template was completely removed, the sample was heated to 500 °C at a rate of 1 °C·min^{-1} and maintained for 3 h in air. The obtained sample with a three-dimensional ordered macroporous structure was denoted as CeO_2-3DOM.

2.2.4. Preparation of CeO_2-Bulk

For comparison, CeO_2-Bulk was prepared. 20 mmol of $Ce(NO_3)_3{\cdot}6H_2O$ and polyethylene glycol (11 000) were mixed in 10 mL ethanol (40 wt%) and magnetically stirred for 2 h to form a transparent homogeneous mixture solution, then dried at 50 °C for 48 h. Finally, the sample was heated to 500 °C at a rate of 1 °C·min^{-1} and maintained for 3 h in air. The obtained sample was denoted as CeO_2-Bulk.

2.3. Material characterizations

The prepared CeO_2-3DOM, CeO_2-NP, and CeO_2-Bulk samples were characterized by nitrogen absorption–desorption, X-ray diffraction (XRD), scanning electron microscopy (SEM), transmission electron microscopy (TEM), hydrogen temperature-programmed reduction (H_2-TPR), oxygen temperature-programmed desorption (O_2-TPD), X-ray photoelectron spectroscopy (XPS), Raman spectroscopy (Raman), electron paramagnetic resonance (EPR), in situ diffuse reflectance infrared Fourier transform spectroscopy (in situ DRIFTS), and density functional theory (DFT). The detailed characterization methods are provided in the Supplementary Material.

2.4. The activity evaluation

The catalytic performance of the catalysts was tested in a fixed bed reactor, while the concentration of toluene was detected by gas chromatography (Shimadzu GC-2014, Japan). The catalyst (0.1 g) was placed in a quartz tube (Φ = 6 mm), and 100 mL·min^{-1} simulated feed gas consisting of 1000 ppm toluene, 21 vol% O_2, and N_2 (as balance), with a weight hourly space velocity (WHSV) of 60 000 mL·g^{-1}·h^{-1}. SCR atmosphere (NO = NH_3 = 500 ppm). The schematic of the experimental device used for the toluene catalytic oxidation is shown in Figure S1.

The toluene conversion ($X_{toluene}$), CO_2 selectivity, and NO conversion were calculated by the following equations:

$$X_{toluene} = \frac{C_{in} - C_{out}}{C_{in}} \times 100\% \quad (1)$$

$$CO_2\ selectivity\ (\%) = \frac{CO_{2out}}{7 \times (C_{in} - C_{out})} \times 100\ \% \quad (2)$$

$$NO_{x\ conversion} = \frac{NO_{x\ in} - NO_{x\ out}}{NO_{x\ in}} \times 100\% \quad (3)$$

where $X_{toluene}$ is the oxidation rate of toluene (%) and C_{in} and C_{out} represent the toluene concentrations (ppm) at the inlet and outlet of the reactor, respectively. CO_{2out} represents the CO_2 concentration (ppm) at the reactor outlet. NO_{xin} and NO_{xout} represent the NO_x concentrations (ppm) at the inlet and outlet of the reactor, respectively.

The apparent activation energy was calculated by the following equations:

$$r_{toluene} = \frac{F_{toluene} \times X_{toluene}}{m_{cat}} \quad (4)$$

$$r_{toluene} = -kc = [-A\ \exp\left(-\frac{E_a}{RT}\right)]c \quad (5)$$

where $r_{toluene}$, $F_{toluene}$, m_{cat}, k, A, E_a, R, and T are the reaction rate ($mol \cdot g^{-1} \cdot s^{-1}$), gas flow rate ($mmol \cdot s^{-1}$), catalyst weight (g), rate constant (s^{-1}), pre-exponential factor, apparent activation energy ($kJ \cdot mol^{-1}$), universal gas constant ($J \cdot mol^{-1} \cdot K^{-1}$), and reactor temperature (K), respectively. To ensure the reliability of the data, each experimental point was tested three times, and the average value was used for plotting.

The turnover frequency (TOF_{Ce}, s^{-1}) is the number of toluene molecules converted per surface-active Ce site per second [26–29], and is defined as follows:

$$TOF_{Ce}(s^{-1}) = \frac{X_{toluene} \times F\ (mmol \cdot s^{-1}) \times C_0}{m_{cat}(g) \times N\ (mmol \cdot g^{-1})} \quad (6)$$

where N represents the number of active sites ($mmol \cdot g^{-1}$), and the H_2 consumption of first main peak (200–500 ℃) was used to estimate the number of surface active sites [30].

3. Results and discussion

3.1. The catalytic performance of the catalysts

The toluene conversions over the CeO_2-NP, CeO_2-3DOM, and CeO_2-Bulk exhibited typical S-shaped curves (Fig. 1A). The toluene conversion increased as the temperature increased from 100 to 300 °C, whereas it increased rapidly when the temperature exceeded 180 °C. Moreover, all the samples displayed good CO_2 yields. The apparent activation energy (E_a) was calculated from the Arrhenius plots (Fig. 1B). The E_a values of CeO_2-NP, CeO_2-3DOM, and CeO_2-Bulk (listed in Table 1) were 52, 73, and 93 kJ/mol, respectively, which is consistent with the activity of the samples. The reaction rate of the samples can be read directly from Fig. 1B and its values are listed in Table S1. Among them, CeO_2-NP exhibited the highest reaction rate for toluene oxidation, demonstrating that toluene oxidation occurred more easily on the CeO_2-NP than on the CeO_2-3DOM and CeO_2-Bulk catalysts. Besides, the TOF of CeO_2-NP, CeO_2-Bulk, and CeO_2-3DOM were calculated at 140 °C (Table 2) and compared with other metal-based catalysts reported previously (Table S1). The comparison results showed that CeO_2-NP exhibts a good low-temperature catalytic activity and a high TOF_{Ce} value (6.4×10^{-4} s^{-1}).

The NO_x conversion of the three samples improved by varying degrees with increasing temperature (Fig. 1C). Among them, CeO_2-NP exhibted the best catalytic performance (69%) at 220 ℃.

The reaction between VOCs and NO_x is widely believed to be an essential cause of secondary pollution [31]. Therefore, it is necessary to investigate the effect of the SCR atmosphere on the catalytic oxidation performance of toluene. Compared with catalytic toluene

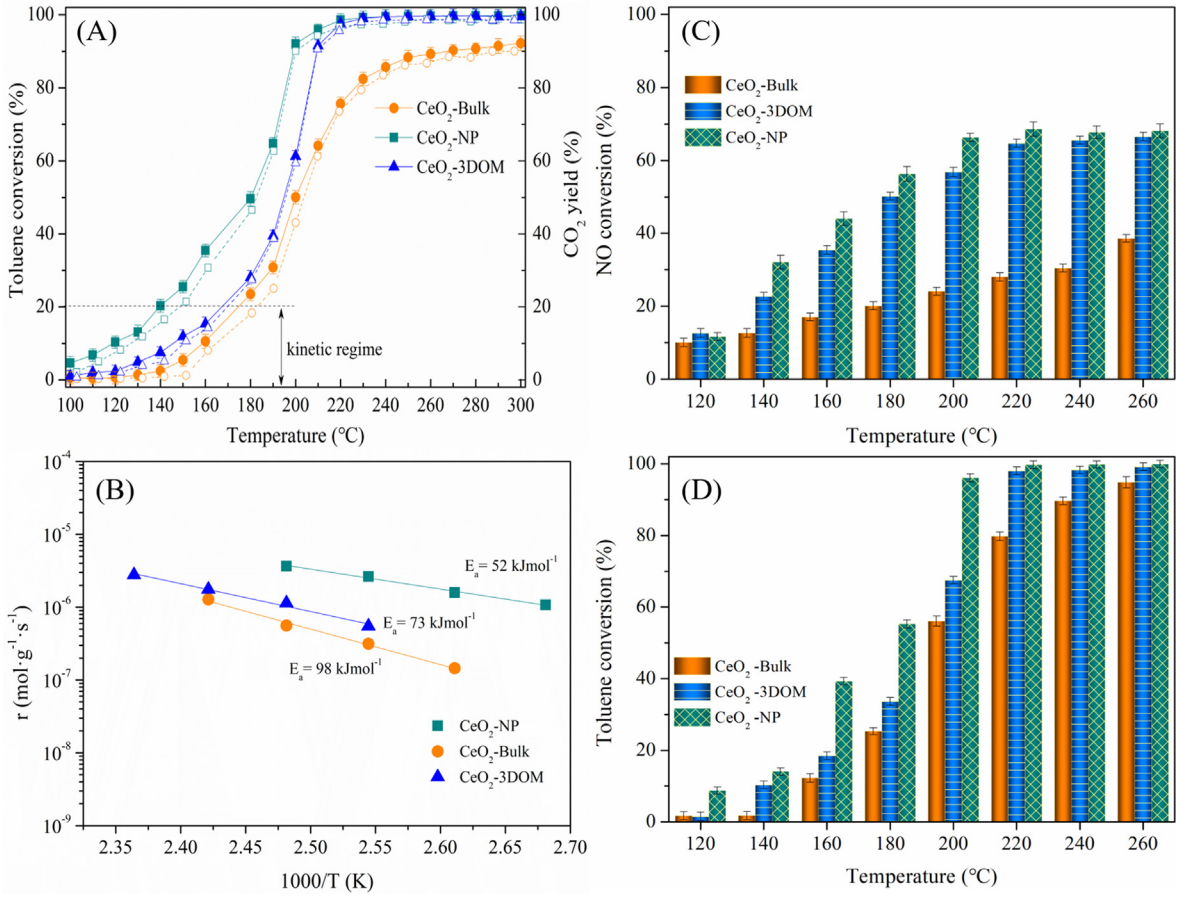

Fig. 1. (A) Catalytic performance of toluene oxidation. (B) Arrhenius plots of toluene oxidation. (C) NO_x conversion. (D) Toluene oxidation in SCR atmosphere.

Table 1
Textural parameters, crystallite size, apparent activation energies (E_a), and the I_{593}/I_{461} ratios from Raman of the samples.

Samples	BET ($m^2 \cdot g^{-1}$)	BJH pore size (nm)	Pore volume ($cm^3 \cdot g^{-1}$)	Crystallite size[a] (nm)	E_a ($kJ \cdot mol^{-1}$)	I_{593}/I_{461} %
CeO_2-Bulk	90	14	0.30	8.5	98	1.7
CeO_2-3DOM	49	12	0.27	7.0	73	1.8
CeO_2-NP	169	7.7	0.28	5.8	52	2.2

[a] Calculated the crystallite size by the Scherrer equation.

Table 2
The results of XPS, H_2 consumption, and TOF_{Ce} values of the samples.

Samples	The relative surface element content (%)				H_2 consumption ($mmol \cdot g^{-1}$)	N[c] ($mmol \cdot g^{-1}$)	TOF_{Ce} ($\times 10^{-4}\ s^{-1}$)
	$Ce^{3+}/(Ce^{3+}+Ce^{4+})$	O_α/O^b_{tot}	O_β/O_{tot}	O_γ/O_{tot}			
CeO_2-Bulk	16	82	18	–	0.61	0.21	0.85
CeO_2-3DOM	18	71	16	13	0.66	0.19	2.9
CeO_2-NP	19	79	21	–	0.78	0.23	6.4
CeO_2-NP-used	16	76	14	10	–	–	–

b represents $O_{tot} = (O_\alpha + O_\beta + O_\gamma)$, [c] represents the number of active sites (Ce), calculated from the hydrogen consumption of the first main peak (200–500 ℃) in the H_2-TPR.

alone (Fig. 1A), the conversion of toluene was promoted to a certain extent over the entire temperature range (120 to 260 ℃) after adding 500 ppm of SCR atmosphere (Fig. 1D). This may be related to the high activity of NO_2, which could promote the reaction with toluene [32].

In addition, the mass transport and heat transfer were calculated using the Weisz-Prater Criterion as described in the Supplementary Material. The Weisz-Prater parameter (N_{W-P}) value was<3, indicating negligible heat transfer or mass transport limitations [33,34].

3.2. Morphological and physical structure analysis

SEM images of the two PMMA templates are shown in Figure S2, while SEM images of CeO_2-NP, CeO_2-3DOM, and CeO_2-Bulk are shown in Fig. 2. CeO_2-Bulk showed an irregular large block morphology, and the structure of its surface was relatively dense (Fig. 2A), with a specific surface area of 90 $m^2 \cdot g^{-1}$. CeO_2-3DOM presented a three-dimensional ordered macroporous structure (Φ = 70–80 nm) (Fig. 2D), giving it a small specific surface area of 49 $m^2 \cdot g^{-1}$. However, the CeO_2-NP catalyst presented a uniform morphology with nanoparticles (Φ = ∼100 nm) and many pores between the particles (Fig. 2G), which contributed to a larger specific surface area (169 $m^2 \cdot g^{-1}$) and provided more active sites for the catalytic reaction of toluene. The SEM images of the CeO_2-Bulk-used (Fig. 2B), CeO_2-3DOM-used (Fig. 2E), and CeO_2-NP-used (Fig. 2H) exhibited similar morphologies to those of the fresh samples, indicating that the cerium-based catalyst has good structural stability even after it has been used.

The morphologies of the CeO_2-Bulk, CeO_2-3DOM, and CeO_2-NP catalysts were more clearly depicted with the aid of HRTEM images, and the results are presented in Fig. 2 C, F, and I. All samples showed clear lattice fringes with an interplanar spacing of 0.32 nm. Meanwhile, the obvious lattice fringe distortions (green rectangles) and crystal defects (red ovals) can be observed [35,36]. Among them, CeO_2-NP presented the highest number of oxygen vacancies.

The N_2 adsorption–desorption isotherm curves are shown in Fig. 3A. CeO_2-NP, CeO_2-3DOM, and CeO_2-Bulk showed IV isotherms with typical H3-type hysteresis loops at 0.1 ∼ 1.0, indicating the mesoporous structures existed in the samples. The pore size distributions of the samples were calculated from the desorption isotherms of the Barrett-Joyner-Halenda (BJH) method (Fig. 3B). In addition, the information on the BET, average pore sizes, and pore volumes are summarized in Table 1. Among them, CeO_2-NP showed the largest surface area (169 $m^2 \cdot g^{-1}$), which conducive to expose more active sites for the oxidation of toluene [37].

Fig. 3C shows the XRD patterns of the CeO_2-NP, CeO_2-3DOM, and CeO_2-Bulk. Three samples exhibited similar diffraction patterns, and the diffraction peaks located at 28.6°, 33.1°, 47.5°, 56.4°, 59.2°, 69.5°, and 76.8° corresponded to the typical cubic fluorite-like structure of CeO_2 [36,38]. The diffraction peaks of CeO_2-NP were weaker than those of CeO_2-3DOM and CeO_2-Bulk, indicating that the crystallite size of CeO_2-NP was smaller than those of CeO_2-3DOM and CeO_2-Bulk [17]. The calculation of crystallite sizes (Table 1) further supports this assumption. The crystallite size was in the order of CeO_2-Bulk (8.5 nm) > CeO_2-3DOM (7 nm) > CeO_2-NP (5.8 nm).

Raman spectroscopy was used to explore the oxygen vacancies on the sample surface (Fig. 3D). The F_{2g} mode observed at ∼ 461 cm^{-1} is the characteristic of the cubic ceria structure of Fm3m fluorite. Besides, a weak peak located at ∼ 593 cm^{-1} belongs to the defect-induced band ("D" band) of the samples. The strength of the "D" band can be used to measure the deformation of the anionic lattice, which could cause punctual defects and oxygen vacancies [39,40]. The I_{593}/I_{461} of CeO_2-NP was higher than those that of CeO_2-Bulk and CeO_2-3DOM (Table 1), indicating that CeO_2-NP had a higher oxygen vacancy concentration than CeO_2-Bulk and CeO_2-3DOM. This is consistent with the HRTEM results.

3.3. Redox behavior, surface metal chemical state, and oxygen species analysis

The H_2-TPR curves of the samples are displayed in Fig. 4A. For CeO_2-3DOM, there are three distinct reduction peaks located at 390, 487, and above 800 °C, corresponding to surface oxygen species, subsurface oxygen species, and bulk oxygen species, respectively [36,41]. The reduction peaks of CeO_2-Bulk were similar to those of CeO_2-3DOM, which can be observed at 364, 472, and 713 °C. However, the reduction peaks of CeO_2-NP were detected at 123, 360, 440, and 695 °C, respectively. Notably, one more peak was detected at 123 °C, with a lower temperature shift of the reduction peaks than CeO_2-Bulk and CeO_2-3DOM. Moreover, CeO_2-NP exhibited the highest H_2 consumption (0.78 $mmol \cdot g^{-1}$, Table 2), indicating that CeO_2-NP possessed more reactive oxygen species and better redox properties.

Subsequently, the reactive oxygen species of the three samples were further determined using O_2-TPD. The peaks in the O_2-TPD curves were classified into three categories: physically adsorbed oxygen (O_{ads}) (<200 °C), chemically adsorbed oxygen (O^{2-} or O_2^-)

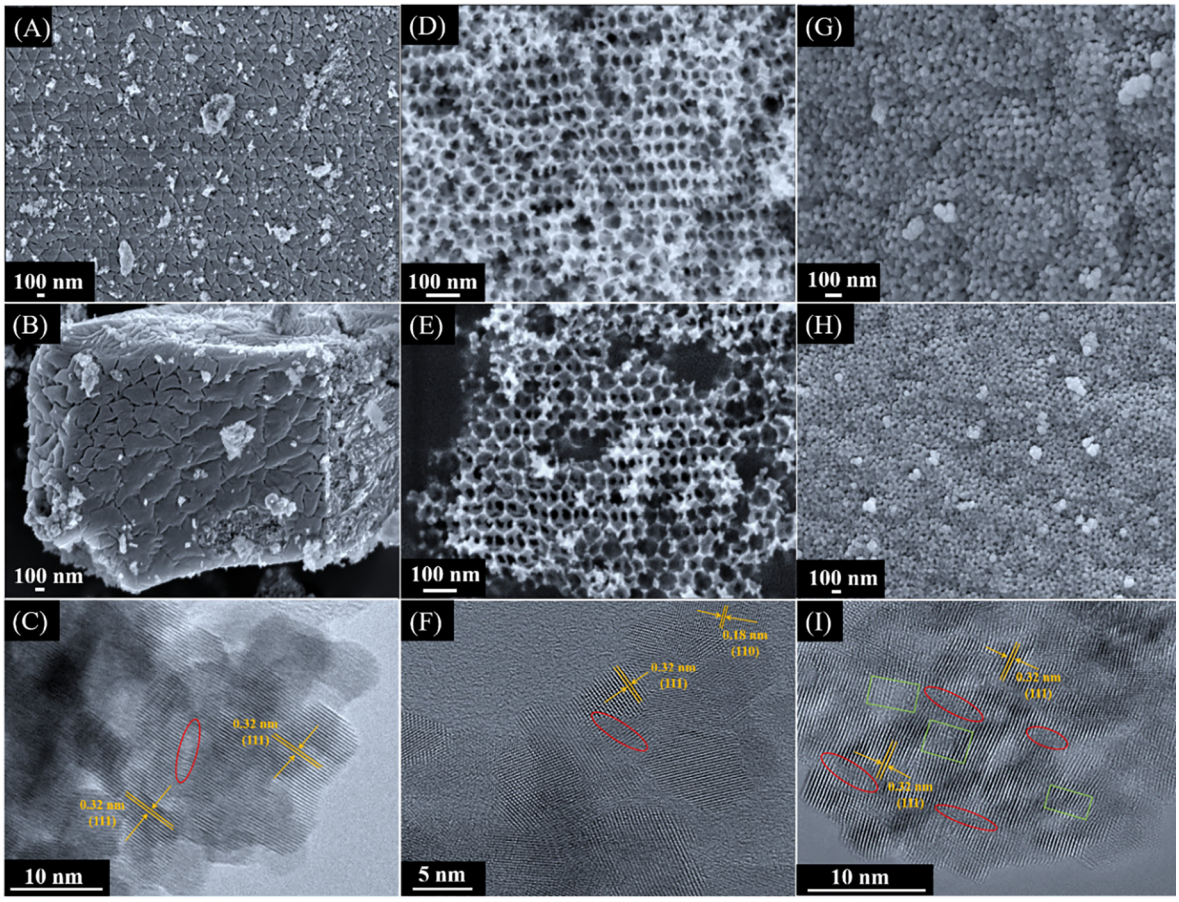

Fig. 2. The SEM image of (A,B) CeO_2-Bulk and CeO_2-Bulk-used, (D,E) CeO_2-3DOM and CeO_2-3DOM-used, (G,H) CeO_2-NP and CeO_2-NP-used. The HRTEM image of (C) CeO_2-Bulk, (F) CeO_2-3DOM, and (I) CeO_2-NP.

(200–400 °C), surface lattice oxygen (O_α) (400–600 °C), and bulk lattice oxygen (>600 °C) [42–45]. Four peaks were observed at 135, 242, 322, and 609 °C over the CeO_2-Bulk (Fig. 4B), which were attributed to O_{ads}, O_2^- or O^-, and O_α, respectively. Three peaks located at 119, 261, and 422 °C over the CeO_2-3DOM catalyst and were attributed to O_{ads}, O_2^- or O^-, and O_α, respectively. Notably, five desorption peaks with larger intensities were observed for the CeO_2-NP. Two more strong peaks at 211 and 707 °C may have been attributed to chemically adsorbed oxygen species and lattice oxygen species, indicating more active oxygen species within CeO_2-NP (O_2, O_2^-, O^{2-}, and O_α) than within CeO_2-Bulk and CeO_2-3DOM. Combined with the above results and previous reports, we can speculate that the type and quantity of active oxygen led to excellent toluene oxidation performance over the CeO_2-NP catalyst.

The XPS measurements were conducted to analyze the surface metal chemical compositions, valence states, and oxygen species of the samples (CeO_2-Bulk, CeO_2-3DOM, CeO_2-NP, and CeO_2-NP-used). Fig. 4C shows the typical Ce 3d XPS spectrum, and in which eight peaks were fitted. The peaks of v′ and u′ were assigned to Ce^{3+}, whereas the others (v, v″, v‴, u, u″, and u‴) were ascribed to Ce^{4+}. The relative surface contents of Ce^{3+} listed in Table 2, and the contents of $Ce^{3+}/(Ce^{3+}+Ce^{4+})$ were 16%, 18%, and 17 % for CeO_2-Bulk, CeO_2-3DOM, and CeO_2-NP, respectively. It has been reported that to maintain electrical neutrality, the higher the Ce^{3+} content, the more oxygen vacancies are formed [5,46]. Oxygen vacancies can generate adsorbed oxygen species to enhance the catalytic performance at lower temperatures [47]. Noteworthy, the relative content of Ce^{3+} within CeO_2-NP-used decreased to 16%, which may have been caused by breaking the cycle between Ce^{3+} and Ce^{4+} after the termination of the reaction (especially cutting off the oxygen supply).

As shown in Fig. 4D, the O 1 s spectra were identified as hydroxyl (OH^-) or absorbed molecular water (O_γ, 532.5 eV), surface-adsorbed oxygen (O_β, 531.3 ~ 531.5 eV), and lattice oxygen (O_α, 528.9 ~ 529.3 eV) [35,48]. The relative contents of the oxygen species are summarized in Table 2. The content of O_α/O_{tot} was 82%, 71%, 79%, and 76% for the CeO_2-Bulk, CeO_2-3DOM, CeO_2-NP, and CeO_2-NP-used, respectively. The molar ratio of O_β/O_{tot}, however, showed the opposite trend in the order CeO_2-NP (21%) > CeO_2-Bulk (18%) > CeO_2-3DOM (16%) > CeO_2-NP-used (14%). CeO_2-NP-fresh had the highest O_β/O_{tot} ratio, which is consistent with the Ce^{3+} content and catalytic activity of the sample. Furthermore, the O_α peak of CeO_2-NP moved to a higher binding energy than those of CeO_2-Bulk and CeO_2-3DOM, thereby indicating lower electronic density. This is significant in facilitating the migration of lattice oxygen species [47]. The activation and migration of lattice oxygen are closely related to oxygen-rich vacancies on the catalyst [26,49]. Thus, oxygen vacancies may play a key role in toluene oxidation over CeO_2-NP at lower temperatures [50–52]. Subsequently, the oxygen vacancy density of the samples was further verified by EPR spectroscopy (Fig. 4E). Compared to CeO_2-Bulk and CeO_2-3DOM, a symmetrical EPR signal (g = 2.003) was observed for CeO_2-NP, which might have been caused by unpaired electrons in the oxygen vacancy sites [53,54]. However, no obvious signal was observed for CeO_2-Bulk and CeO_2-3DOM samples, implying that there are more oxygen vacancies in CeO_2-NP, which is consistent with the Raman and XPS results. The abundance of oxygen vacancies on the CeO_2-NP catalyst is favorable for the activation

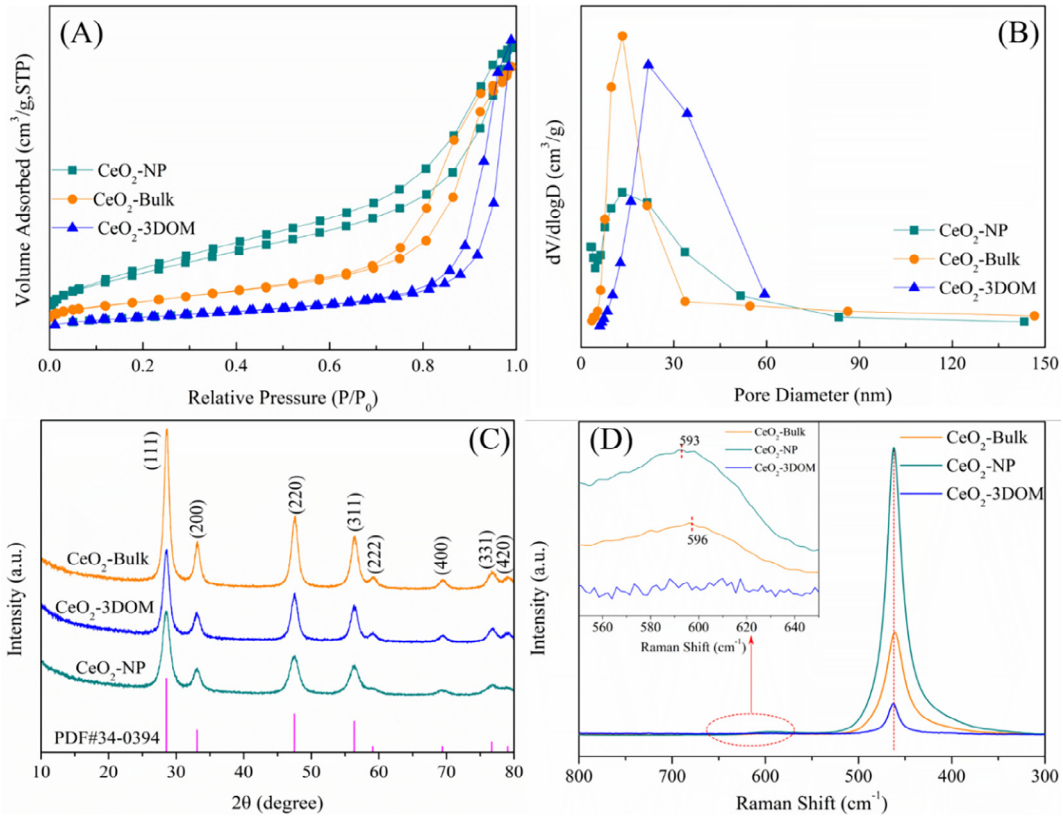

Fig. 3. (A) N_2 adsorption–desorption isotherms, (B) pore size distribution curves, (C) XRD patterns, and (D) Raman spectra.

and migration of lattice oxygen, which is essential for improving the catalytic performance [47,55].

The reaction temperature had a significant influence on the activity of the catalysts. Therefore, it is necessary to study the change in the chemical valence state of surface elements with temperature. CeO_2-NP was selected as the research object and XPS characterization (Figure S3) was performed under the condition of oxygen isolation. The relative surface elemental contents of O_α, O_β, and Ce^{3+} are listed in Table S3. Fig. 4F shows that when the temperature increased from 100 to 260 ℃, the content of O_α decreased from 79% to 62%, while the relative contents of O_β and Ce^{3+} showed an increasing trend from 21% to 38% and from 15% to 21%, respectively. This may be due to the activation and conversion of O_α into O_β during the heating process, and the increase in Ce^{3+} content also contributes to the formation of more O_β, which is consistent with the increasing trend of O_β content. The migration and activation of lattice oxygen are closely related to the oxygen vacancies on the surface of the catalyst and could contribute to toluene oxidation. This implies that O_α and O_β are essential reactive oxygen species in the catalytic reactions [29].

3.4. The investigation of O_2 content, toluene concentration, water vapor, durability, and reusability

The effect of O_2 content on the catalytic performance of CeO_2-Bulk, CeO_2-3DOM, and CeO_2-NP is presented in Fig. 5A. The lowest toluene conversion (<15%) was observed in the absence of oxygen, indicating that oxygen is essential for replenishing oxygen species during catalytic reactions. After 5 vol% O_2 was introduced, the toluene conversions of CeO_2-NP, CeO_2-3DOM, and CeO_2-Bulk increased to 96%, 92%, and 62%, respectively. When the O_2 content increased from 10 vol% to 21 vol%, and the toluene conversion efficiencies of CeO_2-NP, CeO_2-3DOM and CeO_2-Bulk were stable at 63%, 91%, and 97% respectively, indicating that the presence of 5 vol% O_2 was sufficient and could provide a sufficient oxygen concentration during the reaction to maintain an efficient and stable oxidation of toluene. The oxygen transient response experiment results (Figure S4) indicated that gaseous oxygen is essential for toluene oxidation and could rapidly replenish the oxygen species consumed during toluene oxidation [47,56].

The effect of the toluene concentration (500–2000 ppm) on the catalytic activity of CeO_2-NP, CeO_2-3DOM, and CeO_2-Bulk showed that the catalyst had a wide ability to treat toluene (Fig. 5B). In particular, the conversion of CeO_2-NP for toluene has been maintained above 97%.

As the critical parameters, the durability and reusability of the catalyst are of great significance to its application potential for toluene oxidation, which will affect the operation cost in the actual industrialization process. Therefore, long-term durability and stability tests were performed for toluene oxidation over the most promising CeO_2-NP catalyst. Fig. 5C shows the long-term uninterrupted reaction experiment of toluene oxidation under a simulated atmosphere at 210 °C. The oxidation activity of CeO_2-NP to toluene remained unchanged (>99%) during the entire running time of 48 h. In addition, the environment where VOCs exist often contain water vapor at comparably higher concentrations than VOCs. Therefore, the durability of the toluene catalytic oxidation with different water vapors (0, 5, 10, 15, and 20 vol%) over the CeO_2-NP catalysts was investigated. A concentration of 5 vol% H_2O caused a slight decrease in toluene oxidation, while further increasing H_2O content to 10, 15, and 20 vol%, the conversion decreased to 91%, 84%, and 78%, respectively. This implies that water vapor could inhibit the oxidation of toluene, which may be due to the competitive adsorption between toluene and H_2O molecules on the surface of the catalysts [57]. The competitive adsorption could be eliminated after water vapor was removed at the 32nd hour,

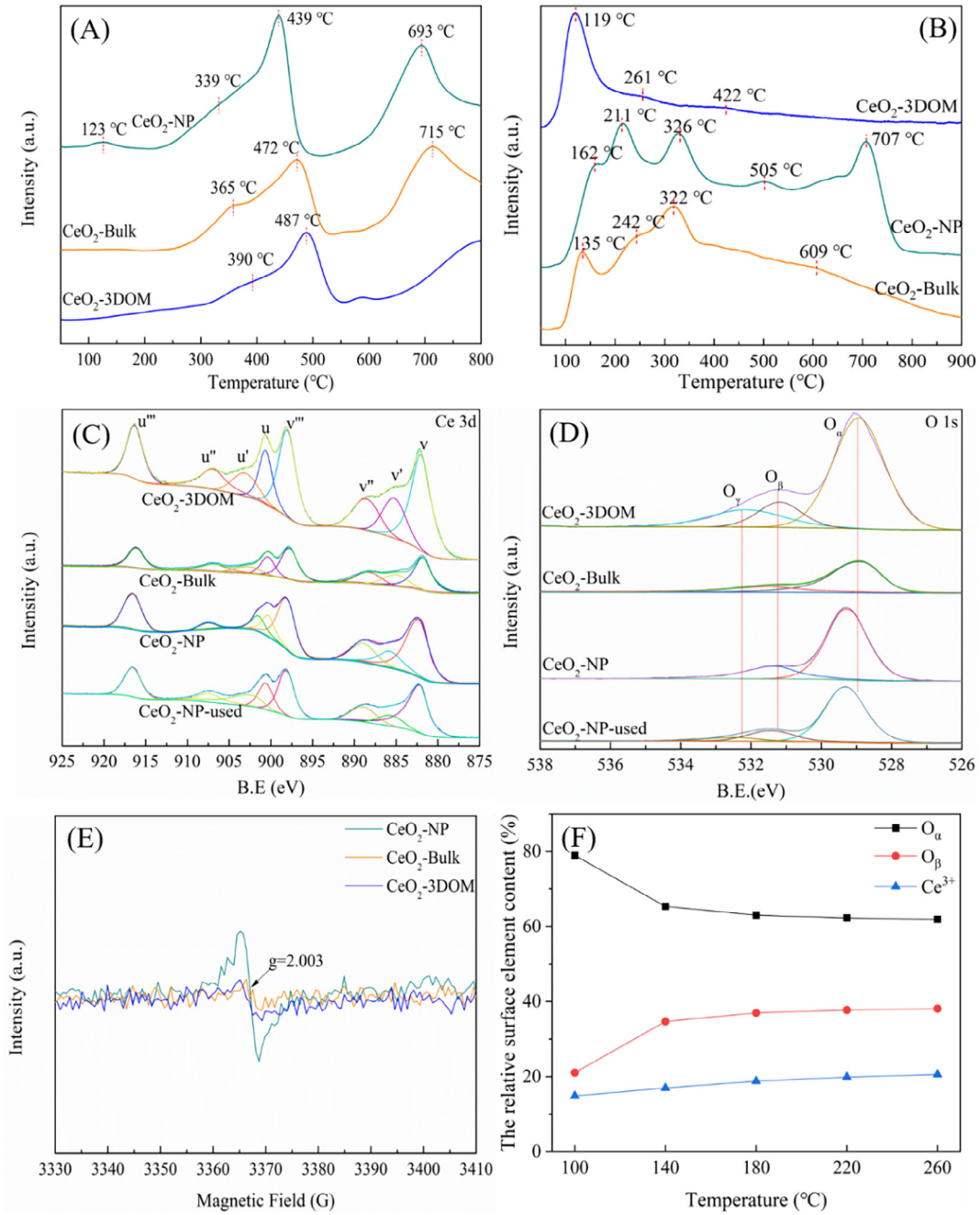

Fig. 4. The H_2-TPR profiles (A) and O_2-TPD profiles (B) of CeO_2-Bulk, CeO_2-3DOM, and CeO_2-NP. (C) Ce 3d XPS spectra, (D) O1s XPS spectra, (E) The EPR spectra, and (F) Effect of temperature on the chemical valence states of surface elements for CeO_2-NP.

indicating that the competitive adsorption between water vapor and toluene had only a temporary inhibitory effect on the toluene oxidation. These results show that CeO_2-NP exhibits excellent water resistance.

Subsequently, the reusability of the CeO_2-NP catalyst was investigated (Fig. 5D), and the toluene oxidation curves were obtained after six consecutive cycles from 140 to 300 °C. As the temperature exceeded 200 °C, the toluene conversion of the CeO_2-NP in each cycle process was higher than 90% and tended to be stable upon increasing temperature. Importantly, its low-temperature activity did not decrease with increasing cycle time, demonstrating that CeO_2-NP had excellent stability for toluene oxidation, making it possible to eliminate toluene in practice. In addition, the experiment of increasing and decreasing reaction temperatures (Figure S5) further showed that the CeO_2-NP catalyst has good stability.

3.5. The exploration of toluene oxidation mechanism over the CeO_2-NP

It is essential to fully understand the intermediate species produced during the oxidation of toluene to further explore the toluene oxidation pathway [27]. Therefore, the in situ DRIFTS experiments on toluene oxidation were performed under N_2 and O_2 atmosphere over the CeO_2-NP catalyst.

Fig. 6A and A1 show the in situ DRIFTS spectra of toluene adsorption at different time intervals over the CeO_2-NP catalyst at 220 °C. The bands at 3027 and 3065 cm^{-1} were assigned to the stretching vibration of C–H bonds in aromatic rings [58]. The

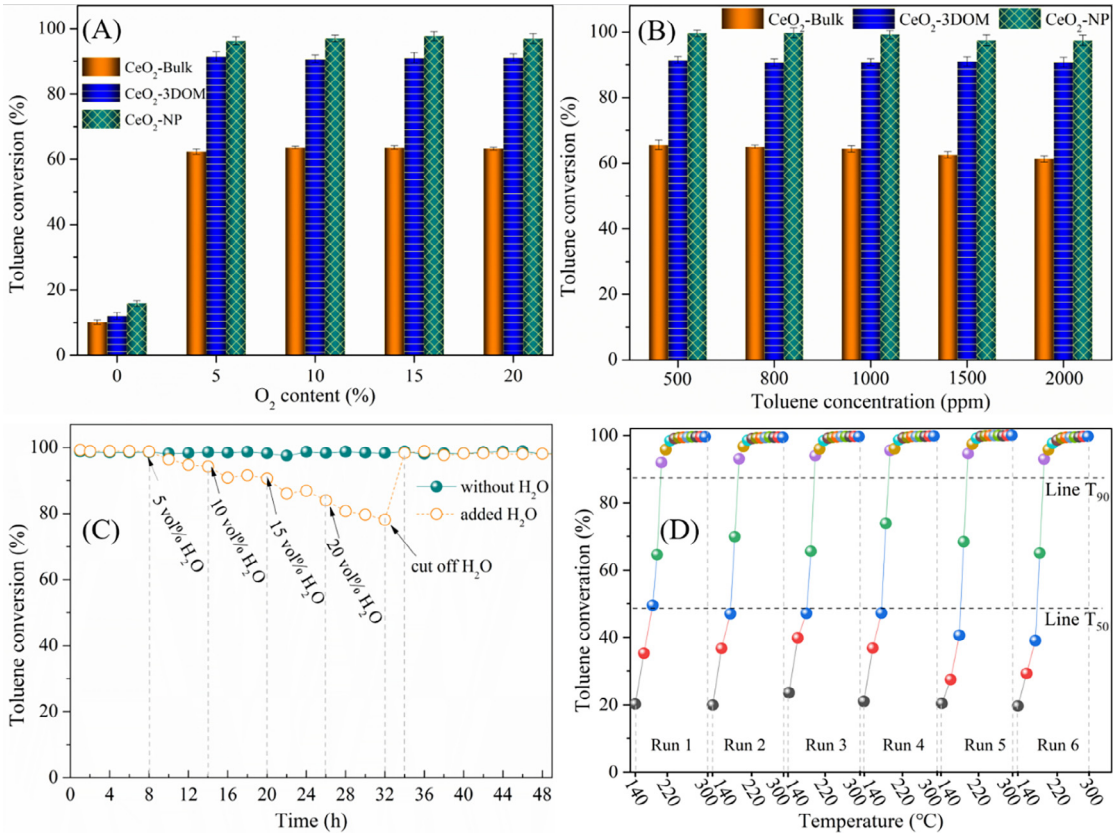

Fig. 5. (A) Effect of O_2 content on toluene oxidation over the samples at 210 °C. (B) Effect of toluene concentration on toluene oxidation over the samples at 210 °C. (C) Durability of CeO_2-NP catalysts for toluene oxidation at 210 °C. (D) Reusability of CeO_2-NP catalysts for toluene oxidation.

bands located at 2845 and 2933 cm^{-1} belong to the stretching vibration of C–H bonds in the alkyl group [26]. The peaks at 1497 and 1589 cm^{-1} were ascribed to the skeleton vibration of C=C in the aromatic ring [57,59]. This indicates that toluene was adsorbed on the surface of the CeO_2-NP. The bands obtained at 1024, 1068, 1157, and 1177 cm^{-1} were corresponded to C-O in benzyl alcohol [60,61]. The characteristic band of benzaldehyde species was observed at 1679 cm^{-1} [62]. The carboxylate groups were detected at 1397, 1428, 1543, and 1559 cm^{-1}, indicating the formation of benzoate species [62,63]. These results suggest that the adsorbed toluene could be oxidized into benzyl alcohol, benzaldehyde, and benzoic acid over CeO_2-NP. In addition, the weak bands found around 1246, 1308, 1814, 1919, and 1959 cm^{-1} corresponded to maleic anhydride [64,65], implying that the aromatic ring was opened. Meanwhile, acetate species were observed at 1360 cm^{-1} [66]. The peak intensity gradually became stronger with the extension of reaction time, indicating that more intermediate species were formed and continuously accumulated on the CeO_2-NP catalyst. The accumulation of intermediate products might be related to the excellent storage and release oxygen function of the CeO_2-NP catalyst, which could provide partial oxygen species for toluene oxidation. This is consistent with the results of the oxygen transient response experiments (Figure S4). As shown in Fig. 6B, the band intensity of intermediate species gradually increased as the temperature increased from 160 to 240 °C, suggesting that higher temperatures were beneficial for the formation of intermediate products. This may be related to the fact that higher temperatures are conducive to the activation of O_α and the formation of more reactive oxygen species. However, no apparent peaks corresponding to CO_2 and H_2O were detected under the condition of N_2 + 1000 ppm toluene, which might be due to the incomplete oxidation of toluene in the absence of oxygen, which that cannot (or rarely can) produce the final products CO_2 and H_2O.

Fig. 6C and D show the change in band intensity with reaction time or temperature in the presence of 21 vol% O_2. The intermediate products detected in the reaction were similar to those observed in the N_2 atmosphere. However, the peak intensity was significantly higher than that in N_2 atmosphere, indicating that more intermediate species were generated and accumulated on the surface of CeO_2-NP. This indicated that the CeO_2-NP catalyst could supply sufficient oxygen species for the oxidation of toluene in the presence of 21 vol% O_2 and accelerated the catalytic degradation of toluene. Compared with Fig. 6B, Fig. 6D highlights that oxygen and high temperature are beneficial for the catalytic oxidation of toluene. When the temperature exceeded 200 °C, the peak intensity remained almost constant, suggesting that the catalytic reaction of toluene almost reached complete conversion at approximately 200 °C, which is in good agreement with the result showing in Fig. 1A for the catalytic performance of toluene oxidation. In addition, absorption peaks corresponding H_2O and CO_2 were found at 1635 and 2316 cm^{-1}, respectively [51,67], indicating that toluene has been indeed oxidized to CO_2 and H_2O.

To obtain a comprehensive understanding of the adsorption process of toluene, DFT + U calculations were combined with in situ DRIFTS. As shown in Fig. S6A, the adsorption energy of toluene over the CeO_2-NP catalyst was −0.51 eV, which means that toluene is more likely to react when its aromatic ring is parallel to the (1 1 1) crystal plane. Moreover, the charge difference density indicated that the electron transfer was more intensified in the methyl group than in the aromatic ring, indicating that the effective activation of the methyl group enhanced charge transfer

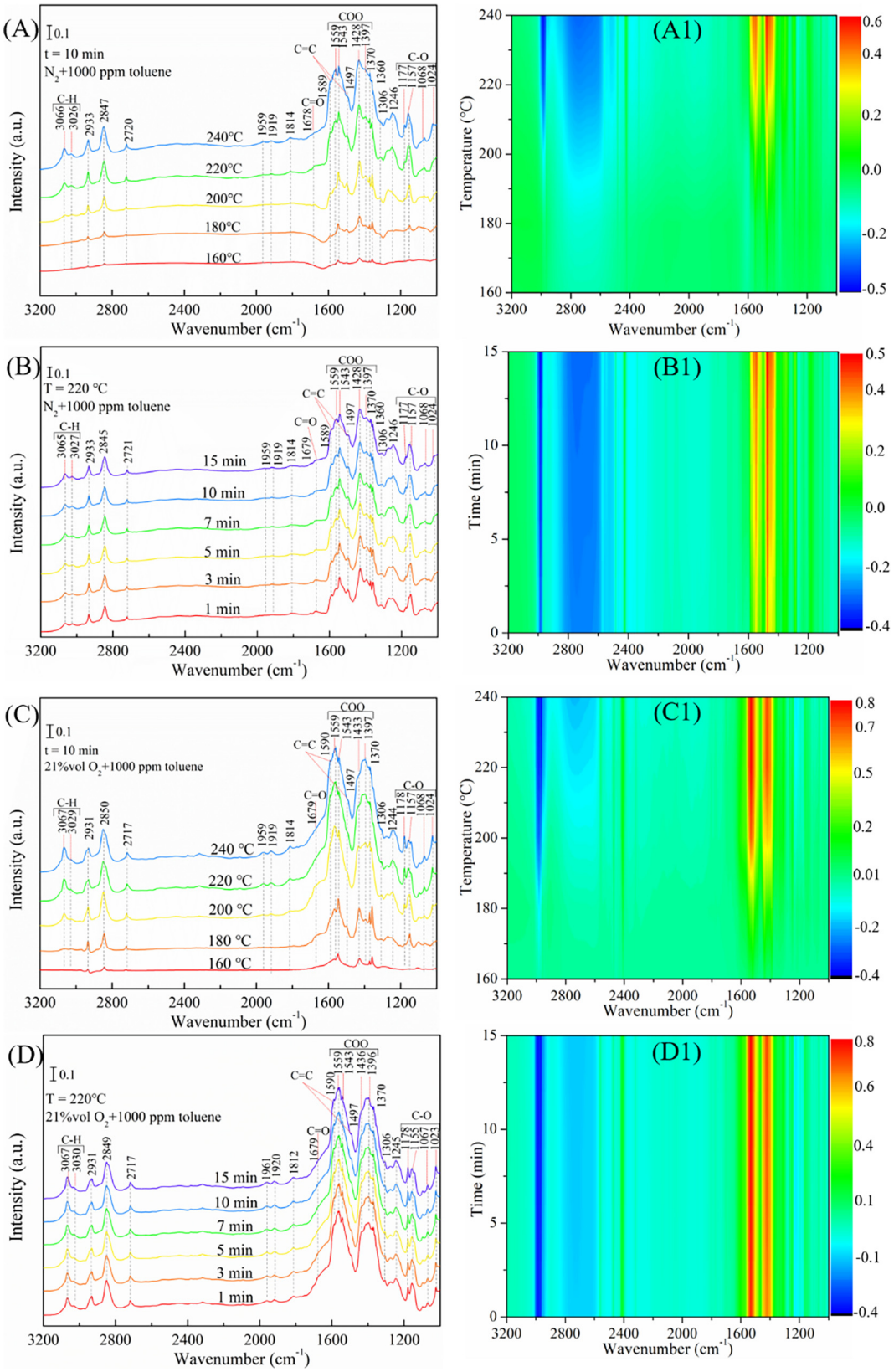

Fig. 6. In situ DRIFTS experiment of toluene oxidation over the CeO_2-NP. (A, A1) N_2 + 1000 ppm toluene at 220 °C. (B, B1) N_2 + 1000 ppm toluene at 160 ~ 240 °C. (C, C1) 21 vol % O_2 + 1000 ppm toluene at 220 °C. (D, D1) 21 vol% O_2 + 1000 ppm toluene at 160–240 °C.

(Fig. S6B). This indicates that the methyl group was more likely to decompose on the CeO_2-NP catalyst than on the benzene ring.

The toluene oxidation mechanism over CeO_2-NP is illustrated in Fig. 7. Toluene was preferentially adsorbed onto the catalyst in the form of an aromatic ring parallel to the reaction plane. The

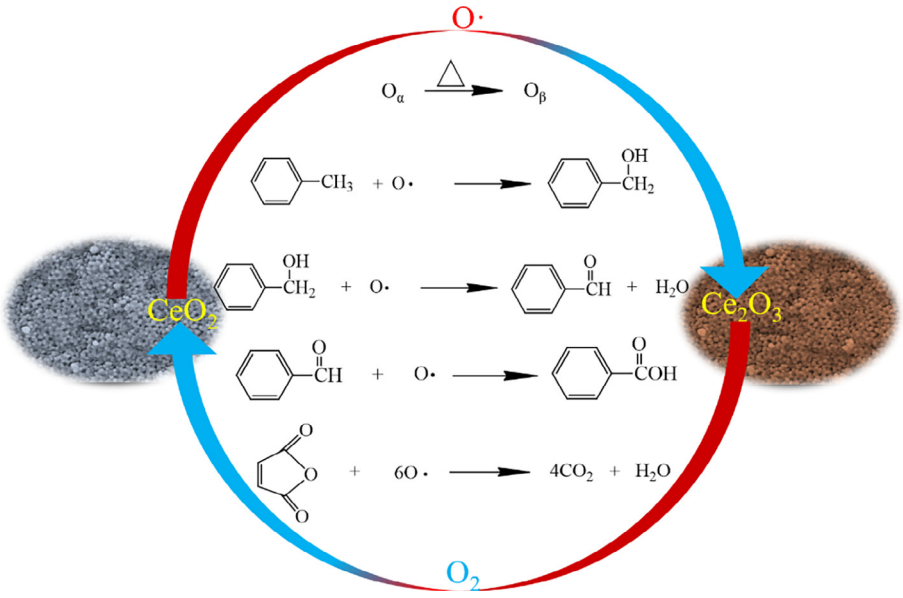

Fig. 7. The toluene oxidation mechanism over CeO_2-NP.

adsorbed toluene was then oxidized successively into benzyl alcohol, benzaldehyde, and benzoic acid with the participation of reactive oxygen species (O_α and O_β). Notably, the presence of oxygen vacancies, a higher temperature was more conducive to activating lattice oxygen and generating sufficient reactive oxygen species to participate in the oxidation reaction of toluene. This plays a crucial role in the catalytic reaction of toluene. Compared to toluene, benzyl alcohol, and benzaldehyde, the aromatic ring-opening process is more likely to occur in benzoic acid because it has the lowest energy barrier [68]. However, the intermediates of small molecules could hardly be detected (except maleic anhydride) after the aromatic ring was opened. This may be because small intermediate species could be oxidized rapidly and barely accumulate on the surface of the CeO_2-NP catalyst. Therefore, it can be inferred that the opening of the aromatic ring is a crucial rate controlling step for the oxidation of toluene [26,60]. Once the aromatic ring was opened, the reaction entered a fast step until the intermediate products were completely oxidized to CO_2 and H_2O. Finally, the gaseous oxygen replenished the active oxygen consumed in the reaction process and entered the next cycle.

4. Conclusions

In summary, the different morphologies of CeO_2 were regulated by template method and successfully applied to the oxidation of toluene at lower temperature. Among them, CeO_2-NP with more oxygen vacancies exhibited the highest efficiency, effectively improving the toluene oxidation performance and broadened the low temperature reaction window. Increasing the temperature is conducive to the activation of O_α, and its conversion into O_β. The fracture of the benzene ring is key to the oxidation of toluene, which is of great significance for guiding the subsequent design of high-performance catalysts. In addition, the remarkable stability and reusability regarding toluene oxidation can effectively reduce the cost of catalysts, making it more possible for CeO_2-NP to eliminate toluene in practice. This work provides a promising strategy for developing a mono-metal catalyst with ideal performance by adjusting the morphology of the catalysts for toluene oxidation at lower temperatures.

CRediT authorship contribution statement

Youcai Zhu: Conceptualization, Methodology, Software, Validation, Investigation, Writing – original draft, Writing – review & editing, Visualization. **Caiting Li:** Conceptualization, Supervision, Resources, Writing – review & editing, Project administration, Funding acquisition, Supervision. **Caixia Liang:** Investigation, Writing – review & editing. **Shanhong Li:** Resources, Investigation, Funding acquisition, Supervision. **Xuan Liu:** Investigation. **Xueyu Du:** Investigation. **Kuang Yang:** Conceptualization, Software. **Jungang Zhao:** Investigation. **Qi Yu:** Investigation. **Yunbo Zhai:** Conceptualization, Software. **Ying Ma:** Conceptualization, Software.

Data availability

Data will be made available on request.

Declaration of Competing Interest

The authors declare that they have no known competing financial interests or personal relationships that could have appeared to influence the work reported in this paper.

Acknowledgments

This work was supported by the National Natural Science Foundation of China (52270102) and the Key Research and Development Program of Hunan Province in China (2018SK2032).

Appendix A. Supplementary material

Supplementary data to this article can be found online at https://doi.org/10.1016/j.jcat.2023.01.012.

References

[1] M.S. Kamal, S.A. Razzak, M.M. Hossain, Catalytic oxidation of volatile organic compounds (VOCs) – a review, Atmos Environ. 140 (2016) 117–134.
[2] C. He, J. Cheng, X. Zhang, M. Douthwaite, S. Pattisson, Z. Hao, Recent advances in the catalytic oxidation of volatile organic compounds: a review based on pollutant sorts and sources, Chem. Rev. 119 (2019) 4471–4568.

[3] Y.T. Lai, T.C. Chen, Y.K. Lan, B.S. Chen, J.H. You, C.M. Yang, N.C. Lai, J.H. Wu, C.S. Chen, Pt/SBA-15 as a highly efficient catalyst for catalytic toluene oxidation, ACS Catal. 4 (2014) 3824–3836.

[4] J. Chen, X. Chen, X. Chen, W.J. Xu, Z. Xu, H.P. Jia, J. Chen, Homogeneous introduction of CeO_y into MnO_x-based catalyst for oxidation of aromatic VOCs, Appl Catal B: Environ. 224 (2018) 825–835.

[5] J.P. Du, Z.P. Qu, C. Dong, L.X. Song, Y. Qin, N. Huang, Low-temperature abatement of toluene over Mn-Ce oxides catalysts synthesized by a modified hydrothermal approach, Appl. Surf. Sci. 433 (2018) 1025–1035.

[6] H. Deng, S. Kang, J. Ma, L. Wang, C. Zhang, H. He, Role of structural defects in MnO_x promoted by Ag doping in the catalytic combustion of volatile organic compounds and ambient decomposition of O_3, Environ. Sci. Technol. 53 (2019) 10871–10879.

[7] S. Xie, J. Deng, S. Zang, H. Yang, G. Guo, H. Arandiyan, H. Dai, Au-Pd/3DOM Co_3O_4: highly active and stable nanocatalysts for toluene oxidation, J. Catal. 322 (2015) 38–48.

[8] L. Liu, J. Li, H. Zhang, L. Li, P. Zhou, X. Meng, M. Guo, J. Jia, T. Sun, In situ fabrication of highly active gamma-MnO_2/$SmMnO_3$ catalyst for deep catalytic oxidation of gaseous benzene, ethylbenzene, toluene, and o-xylene, J. Hazard. Mater. 362 (2019) 178–186.

[9] W. Han, H. Zhao, F. Dong, Z. Tang, Morphology-controlled synthesis of 3D, mesoporous, rosette-like $CeCoO_x$ catalysts by pyrolysis of $Ce[Co(CN)_6]$ and application for the catalytic combustion of toluene, Nanoscale 10 (2018) 21307–21319.

[10] S.H. Xie, J.G. Deng, Y.X. Liu, Z.H. Zhang, H.G. Yang, Y. Jiang, H. Arandiyan, H.X. Dai, C.T. Au, Excellent catalytic performance, thermal stability, and water resistance of 3DOM Mn_2O_3-supported Au-Pd alloy nanoparticles for the complete oxidation of toluene, Appl. Catal. A: Gen. 507 (2015) 82–90.

[11] Y.D. Zhang, C.T. Li, Y.C. Zhu, X.Y. Du, Y. Lyu, S.H. Li, Y.B. Zhai, Insight into the enhanced performance of toluene removal from simulated flue gas over Mn-Cu oxides modified activated coke, Fuel. 276 (2020).

[12] Y. Lyu, C.T. Li, X.Y. Du, Y.C. Zhu, Y.D. Zhang, S.H. Li, Catalytic oxidation of toluene over MnO_2 catalysts with different Mn (II) precursors and the study of reaction pathway, Fuel. 262 (2020).

[13] W. Si, Y. Wang, S. Zhao, F. Hu, J. Li, A facile method for in situ preparation of the MnO_2/$LaMnO_3$ catalyst for the removal of toluene, Environ. Sci. Technol. 50 (2016) 4572–4578.

[14] Y. Wang, L.X. Zhang, L.M. Guo, Enhanced toluene combustion over highly homogeneous iron manganese oxide nanocatalysts, ACS Appl. Nano Mater. 1 (2018) 1066–1075.

[15] Y.N.A. Liao, L.F. He, M.Q. Zhao, D.Q. Ye, Ultrasonic-assisted hydrothermal synthesis of ceria nanorods and their catalytic properties for toluene oxidation, J. Environ. Chem. Eng. 5 (2017) 5054–5060.

[16] Q. Yan, X. Li, Q. Zhao, G. Chen, Shape-controlled fabrication of the porous Co_3O_4 nanoflower clusters for efficient catalytic oxidation of gaseous toluene, J. Hazard. Mater. 209–210 (2012) 385–391.

[17] F.Y. Hu, Y. Peng, J.J. Chen, S. Liu, H. Song, J.H. Li, Low content of CoO_x supported on nanocrystalline CeO_2 for toluene combustion: the importance of interfaces between active sites and supports, Appl. Catal. B: Environ. 240 (2019) 329–336.

[18] Z.T. Feng, M.Y. Zhang, Q.M. Ren, S.P. Mo, R.S. Peng, D.F. Yan, M.L. Fu, L.M. Chen, J.L. Wu, D.Q. Ye, Design of 3-dimensionally self-assembled CeO_2 hierarchical nanosphere as high efficiency catalysts for toluene oxidation, Chem. Eng. J. 369 (2019) 18–25.

[19] P. Yang, S.S. Yang, Z.N. Shi, Z.H. Meng, R.X. Zhou, Deep oxidation of chlorinated VOCs over CeO_2-based transition metal mixed oxide catalysts, Appl. Catal. B: Environ. 162 (2015) 227–235.

[20] M. Yang, G. Shen, Q. Wang, K. Deng, M. Liu, Y. Chen, Y. Gong, Z. Wang, Roles of oxygen vacancies of CeO_2 and Mn-doped CeO_2 with the same morphology in benzene catalytic oxidation, Mole. 26 (2021).

[21] R.L. Mi, D. Li, Z. Hu, R.T. Yang, Morphology effects of CeO_2 Nanomaterials on the catalytic combustion of toluene: a combined kinetics and diffuse reflectance infrared fourier transform spectroscopy study, ACS Catal. 11 (2021) 7876–7889.

[22] A. Ismail, M. Zahid, B. Hu, A. Khan, N. Ali, Y. Zhu, Effect of morphology-dependent oxygen vacancies of CeO_2 on the catalytic oxidation of toluene, Catalyst 12 (2022) 1034.

[23] J.M. López, A.L. Gilbank, T. García, B. Solsona, S. Agouram, L. Torrente-Murciano, The prevalence of surface oxygen vacancies over the mobility of bulk oxygen in nanostructured ceria for the total toluene oxidation, Appl. Catal. B: Environ. 174–175 (2015) 403–412.

[24] L. Heredia, E. Colombo, P. Quaino, S. Collins, Toluene adsorption on CeO_2 (111) studied by FTIR and DFT, Top. Catal. 65 (2022) 934–943.

[25] H. Li, L. Zhang, H. Dai, H. He, Facile synthesis and unique physicochemical properties of three-dimensionally ordered macroporous magnesium oxide, gamma-alumina, and ceria-zirconia solid solutions with crystalline mesoporous walls, Inorg. Chem. 48 (2009) 4421–4434.

[26] W. Yang, Z.a. Su, Z. Xu, W. Yang, Y. Peng, J. Li, Comparative study of α-, β-, γ- and δ-MnO_2 on toluene oxidation: Oxygen vacancies and reaction intermediates, Appl. Catal. B: Environ. 260 (2020) 118150.

[27] S. Ted Oyama, G.-N. Yun, S.-J. Ahn, K.K. Bando, A. Takagaki, R. Kikuchi, How to scrutinize adsorbed intermediates observed by in situ spectroscopy: analysis of coverage transients (ACT), J. Catal. 394 (2021) 273–283.

[28] A. Iino, A. Takagaki, R. Kikuchi, S.T. Oyama, K.K. Bando, Combined in situ XAFS and FTIR study of the hydrodeoxygenation reaction of 2-methyltetrahydrofuran on Ni_2P/SiO_2, J. Phys. Chem. C 123 (2019) 7633–7643.

[29] Y. Qin, H. Wang, C. Dong, Z.P. Qu, Evolution and enhancement of the oxygen cycle in the catalytic performance of total toluene oxidation over manganese-based catalysts, J. Catal. 380 (2019) 21–31.

[30] G.L. Bezemer, J.H. Bitter, H.P.C.E. Kuipers, H. Oosterbeek, J.E. Holewijn, X. Xu, F. Kapteijn, A.J. van Dillen, K.P. de Jong, Cobalt particle size effects in the Fischer-Tropsch reaction studied with carbon nanofiber supported catalysts, J. Am. Chem. Soc. 128 (2006) 3956–3964.

[31] H. Niu, K. Li, B. Chu, W. Su, J. Li, Heterogeneous reactions between toluene and NO_2 on mineral particles under simulated atmospheric conditions, Environ. Sci. Technol. 51 (2017) 9596–9604.

[32] L. Zhao, L. Jiang, Y. Huang, J. Zhang, J. Tang, C. Li, Mechanism investigation of three-dimensional porous A-site substituted $La_{1-x}Co_xFeO_3$ catalysts for simultaneous oxidation of NO and toluene with H_2O, Appl. Surf. Sci. 578 (2022).

[33] S. Oyama, X. Zhang, J. Lu, Y. Gu, T. Fujitani, Epoxidation of propylene with H_2 and O_2 in the explosive regime in a packed-bed catalytic membrane reactor, J. Catal. 257 (2008) 1–4.

[34] S. Xie, Y. Liu, J. Deng, X. Zhao, J. Yang, K. Zhang, Z. Han, H. Arandiyan, H. Dai, Effect of transition metal doping on the catalytic performance of Au-Pd/3DOM Mn_2O_3 for the oxidation of methane and o-xylene, Appl. Catal. B: Environ. 206 (2017) 221–232.

[35] L.L. Zhao, Z.P. Zhang, Y.S. Li, X.S. Leng, T.R. Zhang, F.L. Yuan, X.Y. Niu, Y.J. Zhu, Synthesis of Ce_aMnO_x hollow microsphere with hierarchical structure and its excellent catalytic performance for toluene combustion, Appl. Catal. B: Environ. 245 (2019) 502–512.

[36] F. Hu, J. Chen, Y. Peng, H. Song, K. Li, J. Li, Novel nanowire self-assembled hierarchical CeO_2 microspheres for low temperature toluene catalytic combustion, Chem. Eng. J. 331 (2017).

[37] Y. Luo, Y. Zheng, J. Zuo, X. Feng, X. Wang, T. Zhang, K. Zhang, L. Jiang, Insights into the high performance of Mn-Co oxides derived from metal-organic frameworks for total toluene oxidation, J. Hazard. Mater. 349 (2018) 119–127.

[38] C. He, Y. Yu, Y. Lin, N. Qiao, J. Li, Q. Shen, W. Yu, J. Chen, Z. Hao, Low-temperature removal of toluene and propanal over highly active mesoporous $CuCeO_x$ catalysts synthesized via a simple self-precipitation protocol, Appl. Catal. B: Environ. 147 (2014) 156–166.

[39] M. Lykaki, E. Pachatouridou, S.A.C. Carabineiro, E. Iliopoulou, C. Andriopoulou, N. Kallithrakas-Kontos, S. Boghosian, M. Konsolakis, Ceria nanoparticles shape effects on the structural defects and surface chemistry: Implications in CO oxidation by Cu/CeO_2 catalysts, Appl. Catal. B: Environ. 230 (2018) 18–28.

[40] Q.Y. Wang, K.L. Yeung, M.A. Banares, Operando Raman-online FTIR investigation of ceria, vanadia/ceria and gold/ceria catalysts for toluene elimination, J. Catal. 364 (2018) 80–88.

[41] W. Wang, Q. Zhu, Q.G. Dai, X.Y. Wang, Fe doped CeO_2 nanosheets for catalytic oxidation of 1,2-dichloroethane: Effect of preparation method, Chem. Eng. J. 307 (2017) 1037–1046.

[42] T. Cai, H. Huang, W. Deng, Q.G. Dai, W. Liu, X.Y. Wang, Catalytic combustion of 1,2-dichlorobenzene at low temperature over Mn-modified Co_3O_4 catalysts, Appl. Catal. B: Environ. 166 (2015) 393–405.

[43] L. Deng, Y.P. Ding, B.Q. Duan, Y.W. Chen, P.W. Li, S.M. Zhu, S.B. Shen, Catalytic deep combustion characteristics of benzene over cobalt doped Mn-Ce solid solution catalysts at lower temperatures, Mole. Catal. 446 (2018) 72–80.

[44] Q.M. Ren, S.P. Mo, R.S. Peng, Z.T. Feng, M.Y. Zhang, L.M. Chen, M.L. Fu, J.L. Wu, D.Q. Ye, Controllable synthesis of 3D hierarchical Co_3O_4 nanocatalysts with various morphologies for the catalytic oxidation of toluene, J. Mater. Chem. A. 6 (2018) 498–509.

[45] Y. Wang, D.Y. Yang, S.Z. Li, L.X. Zhang, G.Y. Zheng, L.M. Guo, Layered copper manganese oxide for the efficient catalytic CO and VOCs oxidation, Chem. Eng. J. 357 (2019) 258–268.

[46] X.Y. Feng, J.X. Guo, X.R. Wen, M.Y. Xu, Y.H. Chu, S.D. Yuan, Enhancing performance of Co/CeO_2 catalyst by Sr doping for catalytic combustion of toluene, Appl. Surf. Sci. 445 (2018) 145–153.

[47] Z. Su, W. Yang, C. Wang, S. Xiong, X. Cao, Y. Peng, W. Si, Y. Weng, M. Xue, J. Li, Roles of oxygen vacancies in the bulk and surface of CeO_2 for toluene catalytic combustion, Environ. Sci. Technol. 54 (2020) 12684–12692.

[48] Z. Cheng, Z. Chen, J.R. Li, S.F. Zuo, P. Yang, Mesoporous silica-pillared clays supported nanosized Co_3O_4-CeO_2 for catalytic combustion of toluene, Appl. Surf. Sci. 459 (2018) 32–39.

[49] J.L. Wang, J.E. Li, C.J. Jiang, P. Zhou, P.Y. Zhang, J.G. Yu, The effect of manganese vacancy in birnessite-type MnO_2 on room-temperature oxidation of formaldehyde in air, Appl. Catal. B: Environ. 204 (2017) 147–155.

[50] J. Deng, S. He, S. Xie, H. Yang, Y. Liu, G. Guo, H. Dai, Ultralow loading of silver nanoparticles on Mn_2O_3 nanowires derived with molten salts: a high-efficiency catalyst for the oxidative removal of toluene, Environ. Sci. Technol. 49 (2015) 11089–11095.

[51] J. Chen, X. Chen, W.J. Xu, Z. Xu, J.Z. Chen, H.P. Jia, J. Chen, Hydrolysis driving redox reaction to synthesize Mn-Fe binary oxides as highly active catalysts for the removal of toluene, Chem. Eng. J. 330 (2017) 281–293.

[52] B.E. Petel, W.W. Brennessel, E.M. Matson, Oxygen-atom vacancy formation at polyoxovanadate clusters: homogeneous models for reducible metal oxides, J. Am. Chem. Soc. 140 (2018) 8424–8428.

[53] S.P. Mo, Q. Zhang, J.Q. Li, Y.H. Sun, Q.M. Ren, S.B. Zou, Q. Zhang, J.H. Lu, M.L. Fu, D.Q. Mo, J.L. Wu, H.M. Huang, D.Q. Ye, Highly efficient mesoporous MnO_2 catalysts for the total toluene oxidation: oxygen-vacancy defect engineering and involved intermediates using in situ DRIFTS, Appl. Catal. B: Environ. 264 (2020).

[54] Y.C. Zhang, Z. Li, L. Zhang, L. Pan, X.W. Zhang, L. Wang, J.J.Z. Fazal-e-Aleem, Role of oxygen vacancies in photocatalytic water oxidation on ceria oxide: experiment and DFT studies, Appl. Catal. B: Environ. 224 (2018) 101–108.
[55] F. Esch, S. Fabris, L. Zhou, T. Montini, C. Africh, P. Fornasiero, G. Comelli, R. Rosei, Electron localization determines defect formation on ceria substrates, Science. 309 (2005) 752–755.
[56] Y.N. Liao, L.F. He, C.G. Man, L.M. Chen, M.L. Fu, J.L. Wu, D.Q. Ye, B.C. Huang, Diameter-dependent catalytic activity of ceria nanorods with various aspect ratios for toluene oxidation, Chem. Eng. J. 256 (2014) 439–447.
[57] S. Zhao, F. Hu, J. Li, Hierarchical core-shell Al_2O_3@Pd-CoAlO microspheres for low-temperature toluene combustion, ACS Catal. 6 (2016) 3433–3441.
[58] X. Chen, X. Chen, E.Q. Yu, S.C. Cai, H.P. Jia, J. Chen, P. Liang, In situ pyrolysis of Ce-MOF to prepare CeO_2 catalyst with obviously improved catalytic performance for toluene combustion, Chem. Eng. J. 344 (2018) 469–479.
[59] Z.B. Rui, M.N. Tang, W.K. Ji, J.J. Ding, H.B. Ji, Insight into the enhanced performance of TiO_2 nanotube supported Pt catalyst for toluene oxidation, Catal. Today. 297 (2017) 159–166.
[60] Y. Shen, J. Deng, S. Impeng, S. Li, T. Yan, J. Zhang, L. Shi, D. Zhang, Boosting toluene combustion by engineering Co-O Strength in cobalt oxide catalysts, Environ. Sci. Technol. 54 (2020) 10342–10350.
[61] R.M. Chen, J.Y. Li, J.P. Sheng, W. Cui, X.A. Dong, P. Chen, H. Wang, Y.J. Sun, F. Dong, Unveiling the unconventional roles of methyl number on the ring-opening barrier in photocatalytic decomposition of benzene, toluene and o-xylene, Appl. Catal. B: Environ. 278 (2020).
[62] X. Yang, X. Ma, X. Yu, M. Ge, Exploration of strong metal-support interaction in zirconia supported catalysts for toluene oxidation, Appl. Catal. B: Environ. 263 (2020).
[63] C. Dong, Z.P. Qu, Y. Qin, Q. Fu, H.C. Sun, X.X. Duan, Revealing the highly catalytic performance of spinel $CoMn_2O_4$ for toluene oxidation: involvement and replenishment of oxygen species using in situ designed-TP techniques, ACS Catal. 9 (2019) 6698–6710.
[64] X. Chen, X. Chen, S.C. Cai, J. Chen, W.J. Xu, H.P. Jia, J. Chen, Catalytic combustion of toluene over mesoporous Cr_2O_3-supported platinum catalysts prepared by in situ pyrolysis of MOFs, Chem. Eng. J. 334 (2018) 768–779.
[65] X. Yang, X. Yu, M. Jing, W. Song, J. Liu, M. Ge, Defective $Mn_xZr_{1-x}O_2$ solid solution for the catalytic oxidation of toluene: insights into the oxygen vacancy contribution, ACS Appl. Mater. Interfaces. 11 (2019) 730–739.
[66] X.Y. Wang, Y. Liu, T.H. Zhang, Y.J. Luo, Z.X. Lan, K. Zhang, J.C. Zuo, L.L. Jiang, R.H. Wang, Geometrical-site-dependent catalytic activity of ordered mesoporous co-based spinel for benzene oxidation: In situ DRIFTS study coupled with Raman and XAFS Spectroscopy, ACS Catal. 7 (2017) 1626–1636.
[67] Z.P. Qu, Y.B. Bu, Y. Qin, Y. Wang, Q. Fu, The improved reactivity of manganese catalysts by Ag in catalytic oxidation of toluene, Appl. Catal. B: Environ. 132 (2013) 353–362.
[68] J.Y. Li, X.A. Dong, G. Zhang, W. Cui, W.L. Cen, Z.B. Wu, S.C. Lee, F. Dong, Probing ring-opening pathways for efficient photocatalytic toluene decomposition, J. Mater. Chem. A. 7 (2019) 3366–3374.